

Magnification-independent Histopathological Image Classification with Similarity-based Multi-scale Embeddings

Yibao Sun¹, Xingru Huang^{1*}, Yaqi Wang², Huiyu Zhou³, Qianni Zhang¹

Abstract—The classification of histopathological images is of great value in both cancer diagnosis and pathological studies. However, multiple reasons, such as variations caused by magnification factors and class imbalance, make it a challenging task where conventional methods that learn from image-label datasets perform unsatisfactorily in many cases. We observe that tumours of the same class often share common morphological patterns. To exploit this fact, we propose an approach that learns similarity-based multi-scale embeddings (SMSE) for magnification-independent histopathological image classification. In particular, a pair loss and a triplet loss are leveraged to learn similarity-based embeddings from image pairs or image triplets. The learned embeddings provide accurate measurements of similarities between images, which are regarded as a more effective form of representation for histopathological morphology than normal image features. Furthermore, in order to ensure the generated models are magnification-independent, images acquired at different magnification factors are simultaneously fed to networks during training for learning multi-scale embeddings. In addition to the SMSE, to eliminate the impact of class imbalance, instead of using the hard sample mining strategy that intuitively discards some easy samples, we introduce a new reinforced focal loss to simultaneously punish hard misclassified samples while suppressing easy well-classified samples. Experimental results show that the SMSE improves the performance for histopathological image classification tasks for both breast and liver cancers by a large margin compared to previous methods. In particular, the SMSE achieves the best performance on the BreakHis benchmark with an improvement ranging from 5% to 18% compared to previous methods using traditional features. The sourcecode is publicly available at: https://github.com/sigma10010/histo_img_cls.

Index Terms—Similarity, Multi-scale Embeddings, Contrastive Learning, Deep Learning, Computational Pathology

I. INTRODUCTION

Pathology is benefiting from the progress in medical imaging technology and is developing into digital and computational pathology. It is generally acknowledged that computational pathology leads to a promising future for cancer diagnosis and precise medicine. The use of digitised whole slide images (WSI) [1], also known as digital slides, has made

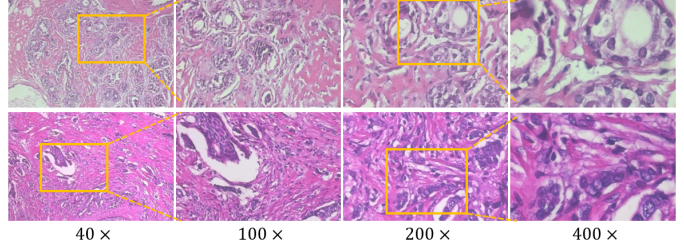


Fig. 1: Histopathological images seen in different magnification factors. Top: benign tumour; bottom: malignant tumour. A yellow bounding box from a smaller magnification level roughly denotes the region of the image seen in next level of magnification.

remote diagnostics possible. However, the visual diagnostic process of WSI examination is still laborious, subjective and error-prone. Thus, automatic computational histopathology analysis is highly demanded for quantitative, objective and reproducible cancer study and diagnostics.

A whole slide image is generally organised in a pyramidal structure that data scanned at different magnification factors are stored at different pyramid levels. Images acquired at a small magnification factor can present meaningful structural information of tissue, but at the same time some cell-level details are lost. In contrast, images acquired at a high magnification factor can capture details of cell components but the corresponding visual field in each region is small. To obtain comprehensive understanding of the WSIs, it is essential to perform image analysis across different magnification levels and jointly exploit the information in them. Fig. 1 illustrates some histopathological images seen in different magnification factors. As it can be seen, these images show in-class visual variability due to the different magnification factors. Besides, more visual variance is also introduced by many aspects in tissue sample staining and scanning conditions. Especially, color variation due to differences in the staining procedure is very common in histopathological images. To illustrate the colour and texture variations within each tissue class, some histopathological images acquired at a magnification factor of 200× from different regions and patients are shown in Fig. 2. For instance, although the first two images belong to the same tubular adenoma (TA) class, different textures are presented in the samples taken from different regions. These appearance variations add significant challenges to

*Corresponding author: Xingru Huang.

¹Yibao Sun, Xingru Huang and Qianni Zhang are with the School of Electronic Engineering and Computer Science, Queen Mary University of London, Mile End Road, London, E1 4NS, United Kingdom (e-mail: yibao.sun; xingru.huang; qianni.zhang@qmul.ac.uk).

²Yaqi Wang is with the College of Media Engineering, Communication University of Zhejiang, Hangzhou, China (e-mail: wangyaqi@cuz.edu.cn).

³Huiyu Zhou is with the School of Informatics, University of Leicester, University Road, Leicester, LE1 7RH, United Kingdom (e-mail: hz143@leicester.ac.uk).

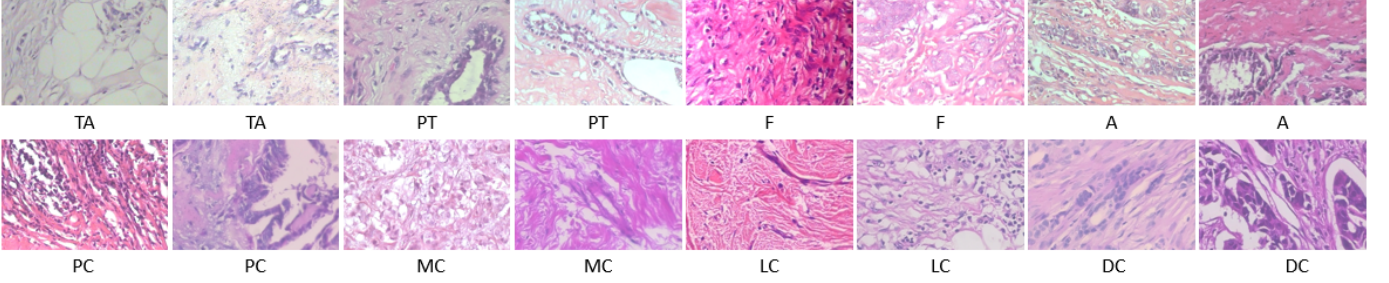


Fig. 2: Histopathological images of different tissue categories acquired at a magnification factor of $200\times$. The top row are benign tumours and bottom are malignant tumours. TA: Tubular Adenoma; PT: Phyllodes Tumour; F: Fibroadenoma; A: Adenosis; PC: Papillary Carcinoma; MC: Mucinous Carcinoma; LC: Lobular Carcinoma; DC: Ductal Carcinoma.

histopathological image classification on top of the variances from multiple magnification scales.

To address this issue, some attempts are made to learn robust features for magnification independent histopathological image classification. In [2], deep learning based features are first extracted from images acquired at different magnification factors and then concatenated together to train magnification independent models. In [3], traditional methods are applied to extract color-texture invariant features and a majority voting approach is used to make final prediction to improve classification performance. Even though deep learning based features learned from image-label structures or those colour-texture invariant features are discriminative in some cases, their performance to identify tumour subtypes still does not reach a satisfactory level in computational pathology due to the in-class variations. It is observed that benign tumours, e.g. TA, PT, F, and A, subtypes in Fig.2, share some common patterns when compared to malignant ones, e.g. PC, MC, LC, DC subtypes. That is to say, tumours of same class (benign or malignant) often appear similar. To exploit this fact in developing effective classification models, we propose a novel representation scheme, similarity-based multi-scale embeddings (SMSE), for magnification-independent histopathological image classification.

Class imbalance is a common problem frequently faced by medical image analysis. Some approaches based on sampling are proposed to address the class imbalance problem for histopathological image classification tasks. For instance, Reza et al. [4] combine different over-sampling and under-sampling methods for imbalanced breast cancer histopathological image classification. An obvious drawback of the sampling-based approaches is that some potentially useful information might be lost in sample discarding. Instead of trying to discard redundant samples for imbalanced histopathological image classification, we propose a dedicated reinforced focal loss to reduce the effect of trivial samples by suppressing the gradients of these samples during training. In this way, the negative impact of the unimportant samples are reduced without losing the useful details.

In this study, we address these challenging issues associated to histopathological image classification. Specifically, we first tackle the difficulties in training magnification-independent classification models by using multi-scale embeddings. Fur-

thermore, we indirectly eliminate the effect of class imbalance by focusing on informative examples during training. The main contributions in this research include: 1) The SMSE scheme that represent images by multi-scale embeddings with contrastive learning. Instead of the conventional image features, multi-scale embeddings learned from image pairs or triplets are proposed to highlight the truly representative features from each class and solve the problem associated to in-class visual variances. 2) A reinforced focal loss function designed for addressing the class imbalance issues in histopathological image classification. Instead of using a sampling strategy, the employment of the reinforced focal loss in learning can simultaneously punish hard misclassified examples while suppressing easy well-classified examples. The problem is solved in a learning and reinforcing manner, to ensure an accurate and flexible selection of information compared to the brute-force sampling of the data.

II. RELATED WORK

A. Histopathological image classification

Classifying tissues in histopathological images is a fundamental step for computational histopathology analysis and of significant value for cancer diagnosis [5], [6]. Efforts have been made to automatically classify histopathological images with different methods including bag of features [7], sparsity model [8], tissue decomposition [9], stacked sparse autoencoder [10], dictionary learning [11] and deep learning [12]–[17]. These methods are usually developed and evaluated on selected data of different sources for pre-defined tasks, and therefore are limited in generalisability and comparability. Furthermore, most of these methods are based on features designed for specific aspects so that these methods can rarely handle the variations due to magnification factors. To take advantage of the common visual features shared by images of a same type of tumour but acquired at different magnification factors, we try to build magnification-independent models based on multi-scale embeddings with contrastive learning for histopathological image classification.

B. Contrastive learning

Contrastive learning is a promising way to learn effective visual representations without human supervision [18]–[20].

These approaches learn visual representations by contrasting positive pairs against negative pairs. To learn from unlabeled data, in [21], the authors propose to treat each instance as a class and perform a variety of transformations to each instance to yield training set with surrogate labels. By using instance classes, human supervision is no longer required. Meanwhile, large computational complexity introduced by learning from instance class pose a new challenge. Memory bank is proposed to tackle the computation load problem [19], [22], [23]. Instead of using a memory bank, some work use in-batch samples for negative sampling [24]–[26]. With pairing samples, distance metrics in an embedding space are used to measured similarity between samples. Similar samples are closer than those dissimilar ones in the embedding space. Various loss functions based on distance metric in an embedding space, such as the contrastive loss [18] and the triplet loss [27], are proposed for similarity learning. Similarity learning is widely used for signature verification [28], one-shot image recognition [29] and object tracking [30], but it is rarely used for histopathological image classification. In this paper, we propose to learn multi-scale embeddings based on a similarity metric for histopathological image classification.

C. Class imbalance

Class imbalance is a very common problem faced by learning visual representation. Common ways to cope with the problem can be grouped into two schemes 1) approaches to balance losses of different samples [31] and 2) approaches to balance samples of different classes [32]. To balance losses, approaches like reweighing schemes [33] and gradient suppression [34] are proposed for different purposes. To balance samples, approaches like active learning [35] and online hard example mining [36] are introduced to select informative samples. In this research, on one hand, considering the convenience of implementation and integrating with other methods, we exploit the first scheme by introducing a loss function to simultaneously reduce losses of easy well-classified samples and increase those of hard misclassified samples. On the other hand, through pairing samples for learning similarity-based embeddings, we indirectly eliminate the impact of the class imbalance problem by controlling the pairing process.

III. FRAMEWORK AND FORMULATION

A. Overview

Fig. 3 depicts the structure of the framework for imbalanced magnification-independent histopathological image classification based on similarity-based multi-scale embeddings (SMSE). It consists of two main phases, i.e., a training phase and a testing phase. The training phase involves three modules. The preprocessing module is developed to generate training sets of image pairs and triplets suitable for contrastive learning. The core SMSE module performs learning of similarity-based multi-scale embeddings. The final classification module entails designs to tackle class imbalance and other problems in image classification.

Instead of being given a single labeled image as the setting for conventional supervised learning, an image pair or triplet

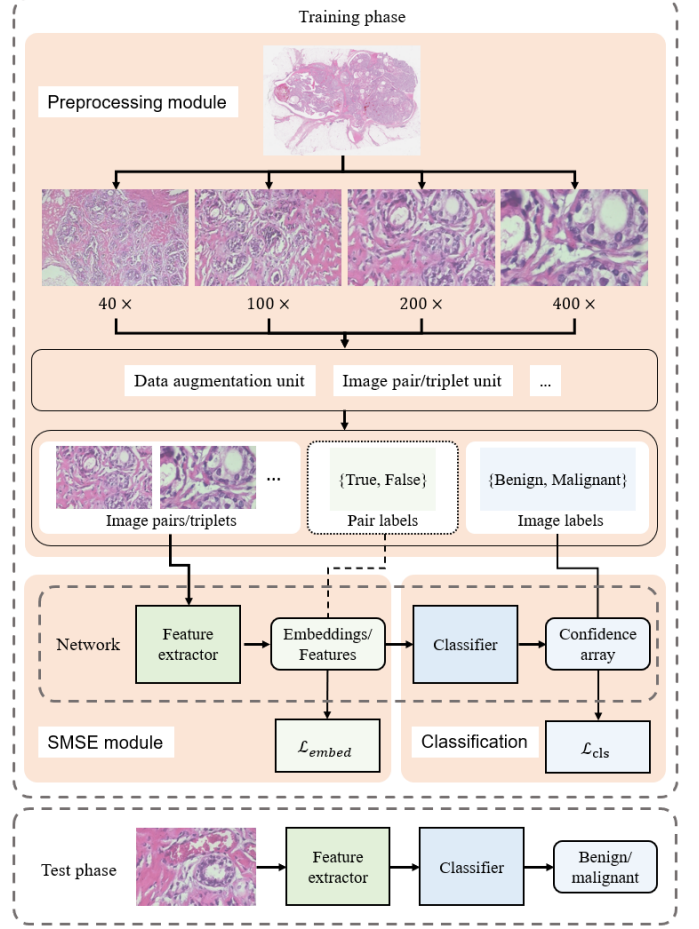


Fig. 3: Framework of learning similarity-based multi-scale embeddings (SMSE) for histopathological image classification. Pair labels in the dotted line box is optional.

is fed to a feature extractor (embedding network) for learning the similarity-based embeddings. The feature extractor can be considered as an embedding function $f(\cdot)$ that maps an input image \mathbf{x} to an embedding ϵ , namely $\epsilon = f(\mathbf{x})$. The learned embedding ϵ then can be fed to train a classifier which mapping an embedding ϵ to a probability distribution p . Instead of training the embedding network and the classifier independently, an end-to-end classification network can be simultaneously trained in a multi-task way. In this case, the objective is to minimize the following hybrid loss function \mathcal{L}_{total} :

$$\mathcal{L}_{total} = \mathcal{L}_{embed} + \mathcal{L}_{cls} \quad (1)$$

where \mathcal{L}_{embed} is for learning similarity-based embeddings (as described in Section III-C) and \mathcal{L}_{cls} for imbalanced image classification (as described in Section III-D). In our experiments, for \mathcal{L}_{embed} , we test either the pair loss Eq. (2) or the triplet loss Eq. (4). For \mathcal{L}_{cls} , we test the proposed reinforced focal loss Eq. (7) compared against the cross-entropy loss function.

B. Preprocessing module

The purpose of the preprocessing module is to generate suitable training datasets. Many tools including a data aug-

mentation unit and an image pair/triplet unit are included to support dataset preparation. To train a magnification-independent classifier, image patches are extracted at different magnification factors from each whole slide image. The data augmentation unit is operated during training to transform the training images in ways of colour jittering, horizontal flipping and vertical flipping with a certain probability of 0.5, to ensure the classifiers are more robust against variations of histology images. For colour jittering, image colour are randomly changed in brightness, contrast, saturation and hue.

The image pair/triplet unit is designed to generate image-pair or image-triplet dataset. Given a conventional image-label dataset $\mathcal{D}_1 = \{(\mathbf{x}_i, y_i) | i \in \mathbb{Z}^+\}$ where \mathbf{x}_i and y_i indicate the i^{th} image and its label respectively, this unit will transform the dataset \mathcal{D}_1 into an image-pair or image-triplet dataset. The process of generating an image-pair dataset from the original image set is summarised in Algorithm 1. A dataset of image pairs is defined as $\mathcal{D}_2 = \{(\mathbf{x}_i, \mathbf{x}'_i, s_i) | i \in \mathbb{Z}^+\}$ where $s_i \in \{0, 1\}$ is a label for i^{th} image pair $(\mathbf{x}_i, \mathbf{x}'_i)$ denoting the similarity between image \mathbf{x}_i and \mathbf{x}'_i , $s_i = 1$ if the paired images \mathbf{x}_i and \mathbf{x}'_i are of same label; otherwise $s_i = 0$. Similarly, Algorithm 2 list the steps for image-triplet dataset generation. A dataset of image triplets is defined as $\mathcal{D}_3 = \{(\mathbf{x}_i^{(a)}, \mathbf{x}_i^{(p)}, \mathbf{x}_i^{(n)}) | i \in \mathbb{Z}^+\}$ where $\mathbf{x}_i^{(a)}$ denotes a reference/anchor image, and $\mathbf{x}_i^{(p)}$ a positive image of a same label as the reference while $\mathbf{x}_i^{(n)}$ a negative image of different label.

Algorithm 1: Image-pair dataset generation

Input: A dataset $\mathcal{D}_1 = \{(\mathbf{x}_i, y_i) | i \in \mathbb{Z}^+\}$;
Initial $\mathcal{D}_2 = \{\}$; $i = 0$;
while $i < \text{size}(\mathcal{D}_1)$ **do**

$i = i + 1$;
 $\mathbf{x}_i \leftarrow i^{th}$ image of \mathcal{D}_1 ;
 $y_i \leftarrow i^{th}$ label of \mathcal{D}_1 ;
 $n \leftarrow$ randomly select $\{0, 1\}$;
if $n = 1$ **then**
 $\quad \mathbf{x}'_i \leftarrow$ randomly select $\mathbf{x}_j \in \mathcal{D}_1$ where $y_j = y_i$;
 $\quad s_i \leftarrow 1$;
 $\quad \mathcal{D}_2 \leftarrow (\mathbf{x}_i, \mathbf{x}'_i, s_i)$;
else
 $\quad \mathbf{x}'_i \leftarrow$ randomly select $\mathbf{x}_k \in \mathcal{D}_1$ where $y_k \neq y_i$;
 $\quad s_i \leftarrow 0$;
 $\quad \mathcal{D}_2 \leftarrow (\mathbf{x}_i, \mathbf{x}'_i, s_i)$;
end

end

Return An image-pair dataset \mathcal{D}_2 .

C. Learning similarity-based multi-scale embeddings

As mentioned before, variations in images at different magnification levels pose significant challenge to histopathological images classification, in addition to the other variation factors due to different regions, patients, labs, procedures, etc. Conventional visual representations are unable to separate benign and malignant tumour, especially when multiple

Algorithm 2: Image-triplet dataset generation

Input: A dataset $\mathcal{D}_1 = \{(\mathbf{x}_i, y_i) | i \in \mathbb{Z}^+\}$;
Initial $\mathcal{D}_3 = \{\}$; $i = 0$;
while $i < \text{size}(\mathcal{D}_1)$ **do**

$i = i + 1$;
 $\mathbf{x}_i^{(a)} \leftarrow i^{th}$ image of \mathcal{D}_1 ;
 $y_i \leftarrow i^{th}$ label of \mathcal{D}_1 ;
 $\mathbf{x}_i^{(p)} \leftarrow$ randomly select $\mathbf{x}_j \in \mathcal{D}_1$ where $y_j = y_i$;
 $\mathbf{x}_i^{(n)} \leftarrow$ randomly select $\mathbf{x}_k \in \mathcal{D}_1$ where $y_k \neq y_i$;
 $\mathcal{D}_3 \leftarrow (\mathbf{x}_i^{(a)}, \mathbf{x}_i^{(p)}, \mathbf{x}_i^{(n)})$;

end

Return An image-triplet dataset \mathcal{D}_3 .

magnification scales are involved in the images. To adequately exploit the common morphology patterns shared by the same tissue type despite of the multi-magnification factors and other visual variations, we propose to learn similarity-based multi-scale embeddings as the main descriptor for histopathological images classification. Advantages behind applying similarity learning are in many folds. First, the embeddings are learned under a constraint that samples of same class are closely clustering and those of different class are separating, and are deemed more descriptive and discriminative than single image based features. Second, through pairing samples for similarity learning, we could indirectly eliminate the impact of the class imbalance problem commonly faced by medical image analysis, by controlling the sampling process. Last but not least, we can generate $O(n^2)$ sample pairs or $O(n^3)$ sample triplets from n training samples, i.e., the training set is significantly augmented during the pairing or tripling process.

Let $\mathbf{x} \in \mathbb{R}^{w \times h \times 3}$ denote an image, and $\epsilon \in \mathbb{R}^{n \times 1}$ an embedding of \mathbf{x} , the similarity between two images \mathbf{x}_1 and \mathbf{x}_2 is then defined as the reciprocal of distance between these two images in the embedding space, namely $\|\epsilon_1 - \epsilon_2\|^{-1}$, where ϵ_1 and ϵ_2 are embeddings for \mathbf{x}_1 and \mathbf{x}_2 respectively and $\|\cdot\|$ is a distance metric. To classify histopathological images according to their similarities, we aim to learn an embedding function $f(\cdot)$ that maps an input image \mathbf{x} into an embedding ϵ so that similar images should cluster closely in the embedding space, namely $\epsilon = f(\mathbf{x}; \Theta)$, where Θ denotes the function's coefficients.

Given an image-pair dataset \mathcal{D}_2 , a pair loss function is proposed to learn similarity-based embeddings, which is defined as:

$$\mathcal{L}_p(\epsilon, \epsilon', s) = \begin{cases} \|\epsilon - \epsilon'\|^2, & \text{if } s = 1 \\ (m - \|\epsilon - \epsilon'\|^2)^+, & \text{if } s = 0 \end{cases} \quad (2)$$

where $(\cdot)^+$ denotes taking positive value or 0, the input variables (ϵ, ϵ', s) are originated from $(\mathbf{x}, \mathbf{x}', s) \in \mathcal{D}_2$ respectively, m is a constant of margin, and $\|\cdot\|$ is the Euclidean distance metric. Now we can fit an embedding function $f(\mathbf{x}; \hat{\Theta}_p)$ on an image-pair dataset \mathcal{D}_2 with the following optimisation:

$$\hat{\Theta}_p = \arg \min_{\Theta} \sum_{(\mathbf{x}_i, \mathbf{x}'_i, s_i) \in \mathcal{D}_2} \mathcal{L}_p(f(\mathbf{x}_i; \Theta), f(\mathbf{x}'_i; \Theta), s_i) \quad (3)$$

After the optimisation, the distance between paired images of different labels should be greater than a margin m in an embedding space.

Given an image-triplet dataset \mathcal{D}_3 , a triplet loss is proposed for learning similarity-based embeddings, which is defined as the following:

$$\mathcal{L}_t(\epsilon^{(a)}, \epsilon^{(p)}, \epsilon^{(n)}) = (\|\epsilon^{(a)} - \epsilon^{(p)}\|^2 - \|\epsilon^{(a)} - \epsilon^{(n)}\|^2 + m)^+ \quad (4)$$

where $(\epsilon^{(a)}, \epsilon^{(p)}, \epsilon^{(n)})$ are embeddings of $(x^{(a)}, x^{(p)}, x^{(n)}) \in \mathcal{D}_3$ respectively. We can then fit another embedding function $f(x; \Theta_t)$ on an image-triplet dataset \mathcal{D}_3 with the following optimisation process:

$$\hat{\Theta}_t = \arg \min_{\Theta} \sum_{(x_i^{(a)}, x_i^{(p)}, x_i^{(n)}) \in \mathcal{D}_3} \mathcal{L}_t(f(x_i^{(a)}; \Theta), f(x_i^{(p)}; \Theta), f(x_i^{(n)}; \Theta)) \quad (5)$$

After the optimisation, the distances between positive pairs should be less than those between negative pairs by a margin m in an embedding space.

The embedding learning process is achieved through the SMSE module in the framework in Fig. 3, in which the loss $\mathcal{L}_{\text{embed}}$ is calculated using either the contrastive loss (\mathcal{L}_p) or the triplet loss (\mathcal{L}_t).

D. A reinforced focal loss function for class imbalance

It is well known that commonly used loss functions for classification tasks, e.g., cross-entropy loss and $L1$ loss, are prone to class imbalance problem due to the overwhelming losses of dominant samples. A common approach to solve the class imbalance problem is to use weighted loss functions where a weighting factor $\alpha \in [0, 1]$ decided by the sample class distribution is introduced to balance the losses of different samples. Instead of applying a weighting balance, some methods like the focal loss attempt to re-design the cross-entropy loss to increase losses of hard samples and decrease those of easy samples [34]. Assuming that a decision boundary for classification is decided by hard samples near to the boundary, the focal loss could to some extent eliminate the effect of class imbalance. However, due to the amplification of logarithmic operation, the cross-entropy loss based focal loss is sensitive to outliers such as wrongly labeled samples which appears regularly in the biomedical imaging domain. The losses of these wrongly labeled samples could be overwhelming.

To address the influence of wrong labels, based on the focal loss, we attempt to re-design the $L1$ loss. Let $p_t \in [0, 1]$ denotes predicted probability of a sample belonging to a ground-truth class, its $L1$ loss \mathcal{L}_{l1} can be calculated as:

$$\mathcal{L}_{l1}(p_t) = 1 - p_t \quad (6)$$

where $p_t \ll 0.5$ stands for hard misclassified samples and $p_t \gg 0.5$ for easy well-classified ones. To simultaneously increase losses of hard samples and decrease those of easy samples, a punishing parameter λ and a suppressing parameter γ are introduced into the $L1$ loss function, as in Eq. (6), to

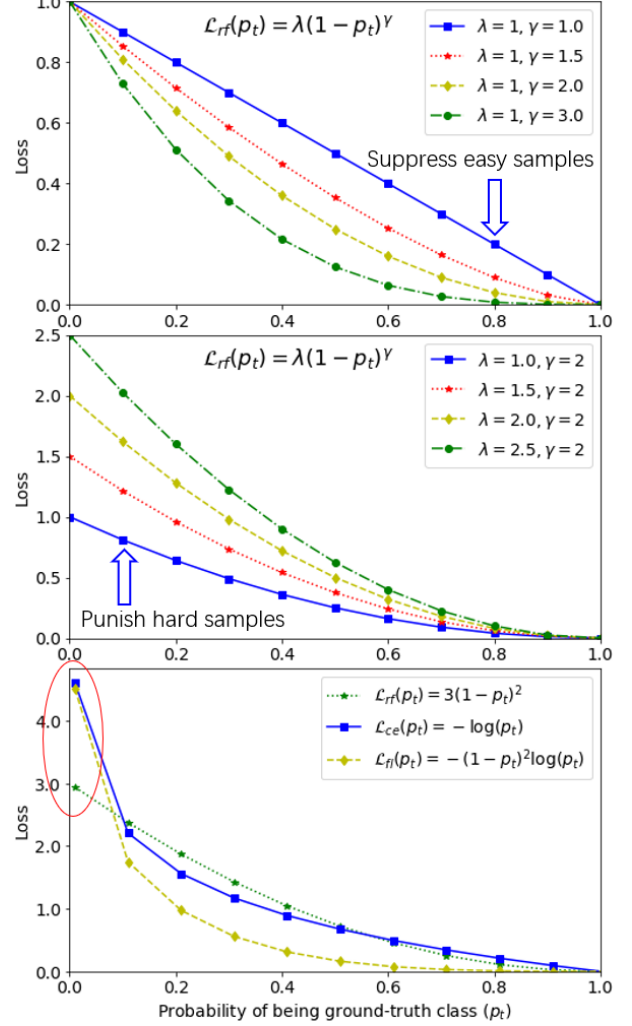


Fig. 4: Curves of the reinforced focal loss function with different combinations of parameters λ and γ . Top: increasing γ to reduce losses of easy well-classified samples. Middle: increasing λ to increase losses of hard misclassified samples. Bottom: the reinforced focal loss compared against the cross-entropy loss and the focal loss. The red circle indicate the cases where the reinforced focal loss is less sensitive to wrongly labeled samples than either the cross-entropy loss or the focal loss.

formulate a new loss function termed as reinforced focal loss $\mathcal{L}_{rf}(\cdot)$:

$$\mathcal{L}_{rf}(p_t) = \lambda(1 - p_t)^\gamma \quad (7)$$

Fig. 4 illustrates the effect of parameter λ for punishing hard samples and γ for suppressing easy samples. Also, the figure shows that the reinforced focal loss is less sensitive to outliers than either the cross-entropy loss or the focal loss. The reinforced focal loss is applied in the classifier (denoted as \mathcal{L}_{cls}) as depicted in the framework and it is shown in the experiments that it can effectively avoid the influence of class imbalance in the target tasks.

IV. EXPERIMENTS AND EVALUATION

In this section, we comprehensively evaluate the performance of the proposed multi-scale histopathology image classification framework, including the SMSE and the reinforced focal loss function in two tasks of breast and liver cancer histopathological image classification.

A. Implementation details

Plain neural networks (PNN) are developed to validate the effectiveness of learning embeddings for histopathological image classification. Implementation details are summarized in Table I. The PNN consists of two modules, an embedding network/feature extractor to map images into embeddings/feature vectors and a classifier to make final class prediction based on input embeddings/feature vectors. Besides the layers listed in the table, there is a non-linear activation layer PReLU following each parametric layer of the embedding network. All the classifiers are trained by the Adam [37] optimizer together with a basic learning rate of 1e-3.

B. Evaluation metrics

Considering variations in images from different patients, patient-wise recognition rate (*RR*) is used for evaluation, which can be expressed as $RR = \frac{1}{N} \sum_{i=1}^N PS_i$, where N is the total number of patients and PS_i denotes i^{th} patient score. The patient score is defined as $PS_i = \frac{N_i^{rec}}{N_i^p}$, where N_i^p denotes the total number of images from i^{th} patient and N_i^{rec} denotes the number of correctly recognised images from i^{th} patient. Also, area under the ROC curve (AUC) and metrics derived from confusion matrix including accuracy ($ACC = \frac{TP+TN}{TP+FP+FN+TN}$) and *F1*-score ($F1 = \frac{2TP}{2TP+FP+FN}$) are used to jointly evaluate breast and liver cancer histopathological image classification.

C. Breast cancer histopathological image classification

The breast cancer histopathological image dataset BreakHis¹ is published for testing and comparing performance for histopathological image classification methods [38]. In this section, we present our experiments applying the plain neural network PNN1 on the BreakHis dataset and validating the effectiveness of the proposed method for breast cancer histopathological image classification.

1) *Dataset description:* The BreakHis dataset contains 7909 breast cancer histopathological images acquired at different magnification factors from 82 patients. Each image has a size of 700×460 pixels and is grouped into either benign (B) or malignant (M) tumour types. Details are summarised in Table II. A patient-wise image splitting protocol is introduced in [38], which guarantees that images from 54 patients are used for training and the remaining from 28 patients for testing. To compare with previous methods tested on the BreakHis dataset, the same 5-fold cross-validation protocol is applied to test the proposed method.

¹<https://web.inf.ufpr.br/vri/databases/breast-cancer-histopathological-database-breakhis/>

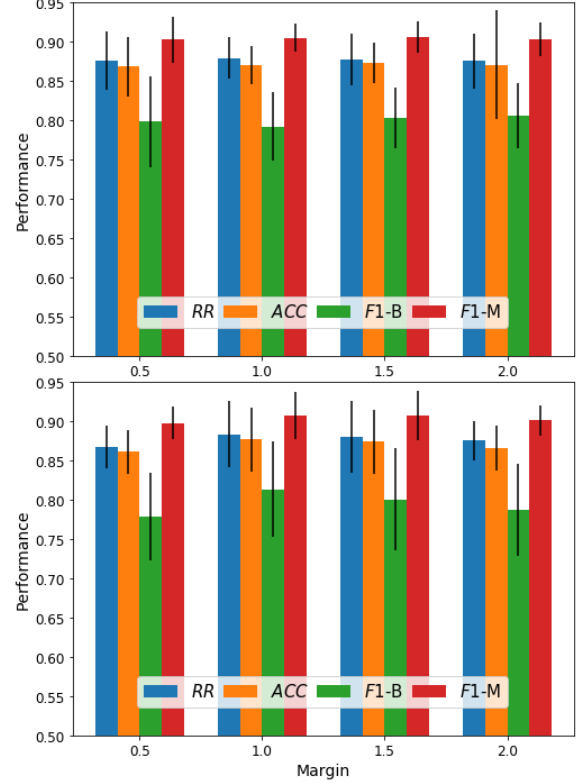


Fig. 5: Classification performance using different margins for the pair loss (top) and the triplet loss (bottom) respectively. *RR*: recognition rate, *ACC*: accuracy, *F1-B*: *F1*-score of benign class, *F1-M*: *F1*-score of malignant class.

2) *Ablation study:* To select the optimal margin m for embedding losses Eq. (2) and (4), we train and evaluate models with the pair and triplet loss functions by varying margin from 0.5 to 2.0 respectively. Table III lists performances of these models evaluated on the BreakHis dataset. To give an intuitive impression, the performance of these models using different margins are also illustrated in a bar chart (Fig. 5). It can be observed that margin $m = 1.0$ for both the pair and triplet losses yields the best overall performance, although differences are minor.

To select the optimal combination of parameters λ and γ in function Eq. 7 for hard example punishing and easy example suppressing, models are trained and evaluated with a series of combinations (λ, γ) . Table IV presents the performance comparison among those models in different combinations. Let $\lambda = 2$, then $\gamma = 1.5$ is an option to yield the best performance while let $\lambda = 3$, the optimal value for γ is 4.0.

To investigate the impact of similarity-based embeddings for histopathological image classification, we test models learned from image pairs or triplets compared to the one learned from single images. Table V lists the performance of these models, similarity-based embeddings learned from image pairs and triplets achieve better classification performance with less standard deviations compared to the conventional features learned from single images. Notably, the SMSE scheme introduces an improvement about 10% in terms of patient-wise

TABLE I: Implementation details of the plain neural networks, which are named as PNN1 and PNN2 with different input sizes for tasks of breast cancer and liver cancer classification respectively.

Component	Layer type	PNN1			PNN2		
		Layer size @stride	Output size	Accumulated depth	Layer size @stride	Output size	Accumulated depth
Embedding network/ Feature extractor	convolution	3 × 5@1	696 × 458 × 4	1	5 × 5@1	220 × 220 × 8	1
	max pooling	2 × 3@2	347 × 229 × 4	1	2 × 2@2	110 × 110 × 8	1
	convolution	3 × 5@1	343 × 227 × 4	2	5 × 5@1	106 × 106 × 16	2
	max pooling	2 × 3@2	171 × 113 × 4	2	2 × 2@2	53 × 53 × 16	2
	convolution	3 × 5@1	167 × 111 × 8	3	5 × 5@1	49 × 49 × 32	3
	max pooling	2 × 3@2	83 × 55 × 8	3	2 × 2@2	24 × 24 × 32	3
	convolution	3 × 5@1	79 × 53 × 16	4	5 × 5@1	20 × 20 × 64	4
	max pooling	2 × 3@2	39 × 26 × 16	4	2 × 2@2	10 × 10 × 64	4
	convolution	3 × 5@1	35 × 24 × 32	5	-	-	-
	max pooling	2 × 3@2	17 × 12 × 32	5	-	-	-
	convolution	3 × 5@1	13 × 10 × 64	6	-	-	-
	max pooling	2 × 3@2	6 × 5 × 64	6	-	-	-
	linear	(1920, 256)	256	7	(6400, 256)	256	5
	linear	(256, 256)	256	8	(256, 256)	256	6
	linear	(256, 12)	12	9	(256, 12)	12	7
Classifier	linear	(12, 2)	2	10	(12, 2)	2	8
	softmax	-	2	10	-	2	8

TABLE II: A summary of the BreakHis dataset.

Class	Magnification factor				Total
	40×	100×	200×	400×	
Benign (B)	625	644	623	588	2480
Malignant (M)	1370	1437	1390	1232	5429
Total	1995	2081	2013	1820	7909

TABLE III: Classification performance of different margins m for the pair loss \mathcal{L}_p (No. 1) and the triplet loss \mathcal{L}_t (No. 2) respectively.

No.	m	RR	ACC	F1-score	
				Benign	Malignant
1	0.5	0.877±0.037	0.869±0.038	0.798±0.058	0.903±0.029
	1.0	0.880±0.026	0.870±0.025	0.792±0.044	0.906±0.018
	1.5	0.878±0.033	0.874±0.026	0.803±0.038	0.906±0.020
	2.0	0.876±0.035	0.871±0.027	0.806±0.041	0.903±0.021
2	0.5	0.867±0.027	0.861±0.028	0.779±0.055	0.898±0.020
	1.0	0.884±0.042	0.877±0.040	0.814±0.061	0.908±0.030
	1.5	0.880±0.046	0.875±0.041	0.800±0.065	0.908±0.031
	2.0	0.876±0.025	0.866±0.029	0.788±0.059	0.902±0.019

recognition rate (RR) and overall accuracy (ACC). Moreover, as illustrated in Fig. 6, the value of $F1$ -B of the conventional method without embeddings changes dramatically due to class imbalance in the BreakHis dataset. Overall, the SMSE scheme works effectively for histopathological breast cancer image classification.

To validate effectiveness of the reinforced focal loss for imbalanced histopathological image classification, we train the

TABLE IV: Performance of different combinations of parameter λ and γ .

(λ, γ)	RR	ACC	F1-score	
			Benign	Malignant
(2, 1.2)	0.870±0.038	0.862±0.039	0.765±0.094	0.900±0.027
(2, 1.5)	0.884±0.042	0.877±0.040	0.814±0.061	0.908±0.030
(2, 2.0)	0.874±0.041	0.864±0.042	0.789±0.069	0.900±0.031
(3, 3.0)	0.872±0.028	0.865±0.026	0.783±0.046	0.901±0.021
(3, 4.0)	0.879±0.036	0.871±0.036	0.797±0.056	0.905±0.027
(3, 5.0)	0.841±0.087	0.833±0.084	0.720±0.173	0.879±0.056

TABLE V: Performance of models trained with or without embeddings ϵ .

w/o ϵ	RR	ACC	F1-score	
			Benign	Malignant
Triplet	0.884±0.042	0.877±0.040	0.814±0.061	0.908±0.030
Pair	0.880±0.026	0.870±0.025	0.792±0.044	0.906±0.018
-	0.793±0.087	0.775±0.099	0.511±0.309	0.851±0.058

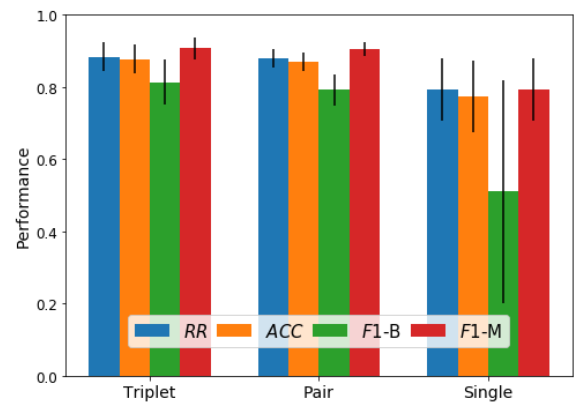


Fig. 6: Classification performance of models trained with image triplets and pairs compared to conventional method that learning from single image.

models with the reinforced focal loss and the cross-entropy loss functions respectively. Fig. 7 depicts the receiver operating characteristic (ROC) [39] curves for different loss functions. As it can be seen from the figures, the reinforced focal loss function achieves a greater mean area under the ROC curve (AUC) with a smaller standard deviation than those of cross-entropy loss function (0.91 ± 0.03 VS 0.89 ± 0.05).

3) *Comparison against the state-of-the-arts:* According to the ablation study (Section IV-C2), we now have an optimal configuration that yields the best overall performance for the BreakHis benchmark. Table VI lists the performance of the model with optimal configurations for reference.

Several traditional methods for feature extraction are eval-

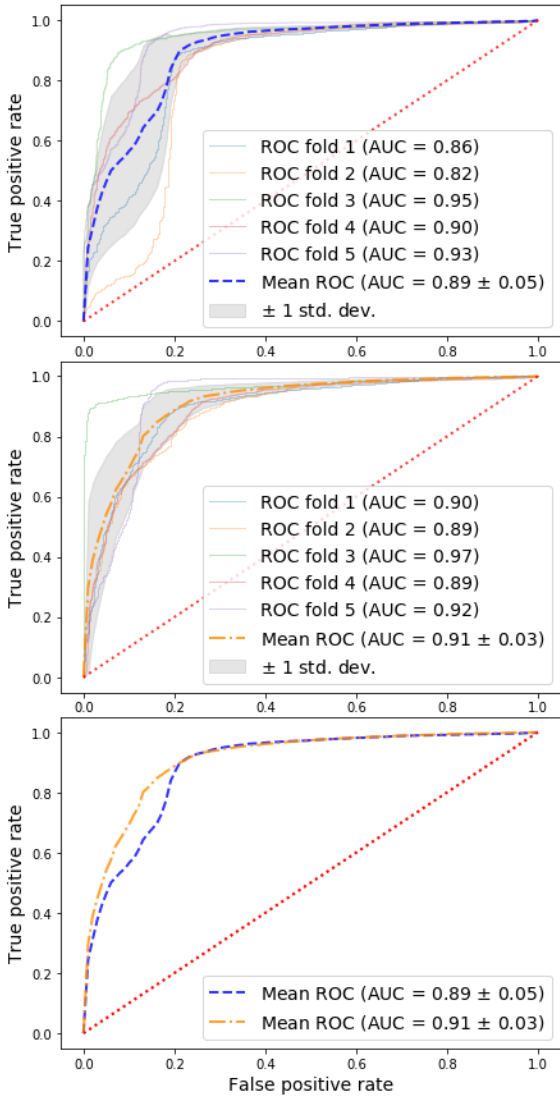


Fig. 7: The ROC curves for different loss functions. Top: cross-entropy loss function, middle: reinforced focal loss function, bottom: comparison.

TABLE VI: Cross-validated performance of model with optimal configurations evaluated on the BreakHis dataset.

Fold	RR (%)	ACC (%)	F1-score (%)	
			Benign	Malignant
1	86.27	85.71	79.59	89.01
2	85.46	83.35	73.26	87.92
3	92.29	92.51	88.42	94.46
4	83.61	84.36	77.09	88.13
5	94.38	92.54	88.48	94.48
<i>Mean ± st.d.</i>	88.40 ± 4.17	87.69 ± 4.01	81.37 ± 6.12	90.80 ± 3.02

uated on the BreakHis dataset in [38], including oriented fast and rotated BRIEF (ORB) [40], local phase quantization (LPQ) [41], local binary patterns (LBP) [42], completed local binary pattern (CLBP) [43], gray-level co-occurrence matrices (GLCM) [44], and parameter-free threshold adjacency statistics (PFTAS) [45]. Furthermore, recently developed deep learning based methods of convolutional neural networks (CNN) [2] and majority voting (MV) [3] achieve the state-of-the-art performance on the BreakHis benchmark. Table VII lists the mean recognition rates and their standard deviations of these methods. In the last row, the results of the proposed SMSE framework is presented, achieving the best overall performance compared to the state-of-the-art. Besides, most of the methods achieve their better recognition rate on images acquired at intermediate magnification factors ($100\times$ and $200\times$) than that either on the low magnification factor ($40\times$) or on the high magnification factor ($400\times$), revealing an interesting fact that image textures at middle magnification levels are relatively more suitable for cancer categorising.

4) *Misclassified analysis*: To further analyse the patient-wise recognition performance, we list individual patient scores of one of the well trained classifiers in Table VIII. From the table we can see that although mean patient scores are satisfactory, the classifier does not perform equally well in all cases. Some underperforming cases include those of patient IDs 10, 11, 24. In particular, 74 out of 95 images are misclassified for patient 24. To better understand the reason for incorrect predictions, we visualise some misclassified benign samples from patient 4 (Fig. 8) and malignant samples from patient 24 (Fig. 9). It can be observed that most misclassified benign samples are acquired at a small magnification factor of $40\times$ and importantly, the misclassified malignant samples contain multiple types of tissue simultaneously. According to these observations, we argue that one possible way to improve patient-wise scores is to introduce further majority voting on patient-wise prediction.

D. Liver cancer histopathological image classification

To further validate the effectiveness of the SMSE framework for histopathological image classification, digital slides of liver cancer from PAIP 2019² are also used for model training and evaluation. In this section, we test and compare the proposed method for the plain neural network PNN2 and networks that have outstanding power for feature extraction, including the GoogleNet [46] and ResNet [47].

1) *Dataset description*: The PAIP 2019 dataset contains 50 liver cancer slides in total, 30 out of 50 are randomly selected for training purpose and the rest 20 are used for testing. Since the PAIP dataset is originally prepared for tasks of tumour segmentation, a ground-truth binary mask to denote viable tumour area is provided for each slide. Each whole slide image is cropped into small patches of size 224×224 pixels for classification purpose. Patches cropped within the viable tumour area are labeled as tumour while the others are labeled as normal. Due to high resolution of whole slide images, excessive patches are produced even by

²<https://paip2019.grand-challenge.org/Dataset/>

TABLE VII: Mean recognition rate (RR) and standard deviation of different methods for classifying histopathological images acquired at different magnification factors.

No.	Method	RR (%)				Average
		40 \times	100 \times	200 \times	400 \times	
1	ORB [40]	74.4 \pm 1.7	69.4 \pm 0.4	69.6 \pm 3.0	67.6 \pm 1.2	70.25 \pm 1.58
2	LPQ [41]	73.8 \pm 5.0	72.8 \pm 5.0	74.3 \pm 6.3	73.7 \pm 5.7	73.65 \pm 5.50
3	LBP [42]	75.6 \pm 2.4	73.2 \pm 3.5	72.9 \pm 2.3	73.1 \pm 5.7	73.70 \pm 3.48
4	CLBP [43]	77.4 \pm 3.8	76.4 \pm 4.5	70.2 \pm 3.6	72.8 \pm 4.9	74.20 \pm 4.20
5	GLCM [44]	74.7 \pm 1.0	78.6 \pm 2.6	83.4 \pm 3.3	81.7 \pm 3.3	79.60 \pm 2.55
6	PFTAS [45]	83.8 \pm 2.0	82.1 \pm 4.9	85.1 \pm 3.1	82.3 \pm 3.8	83.33 \pm 3.45
7	CNN [2]	83.08 \pm 2.08	83.17 \pm 3.51	84.63 \pm 2.72	82.10 \pm 4.42	83.25 \pm 3.18
8	MV [3]	87.20 \pm 3.74	88.22 \pm 3.28	88.89 \pm 2.51	85.82 \pm 3.81	87.53 \pm 3.34
9	Proposed SMSE	87.51\pm4.07	89.12\pm2.86	90.83\pm3.31	87.10\pm3.80	88.64\pm3.51

TABLE VIII: Patient-wise recognition. N^p : number of images from different patients, N^{rec} : number of correctly recognised images, PS : patient score, B: benign, M: malignant.

ID	1	2	3	4	5	6	7	8	9	10	11	12	13	14	15	16	17	18	19	20	21	22	23	24	25	26	27	28
Class	M	M	M	B	M	M	M	M	M	M	M	B	M	B	B	B	M	M	B	B	M	M	M	M	M	M		
N^p	146	123	119	94	125	87	74	45	108	64	65	142	64	98	65	132	158	81	57	84	59	61	66	95	44	88	78	155
N^{rec}	145	110	119	78	125	86	74	44	108	44	41	142	64	84	65	126	142	81	54	84	59	61	66	21	44	88	76	153
$PS(%)$	99	89	100	83	100	99	100	98	100	69	63	100	100	86	100	95	90	100	95	100	100	100	100	22	100	100	97	99

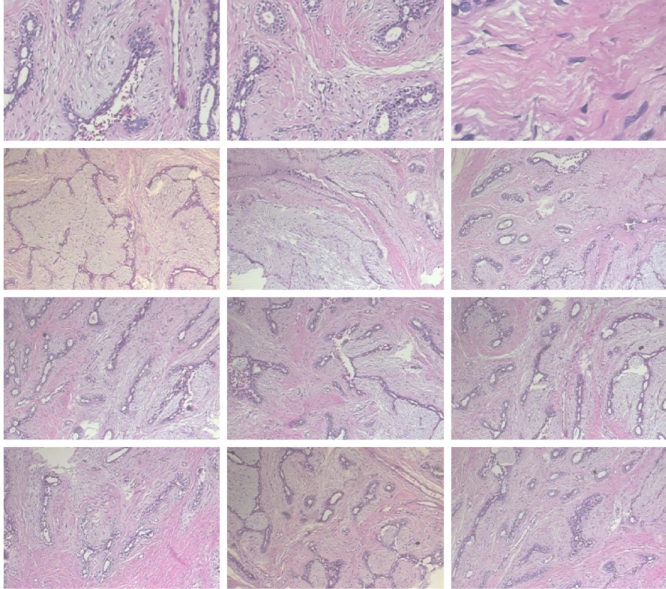


Fig. 8: Misclassified benign samples. Most samples are acquired at a magnification factor of 40 \times except the top three.

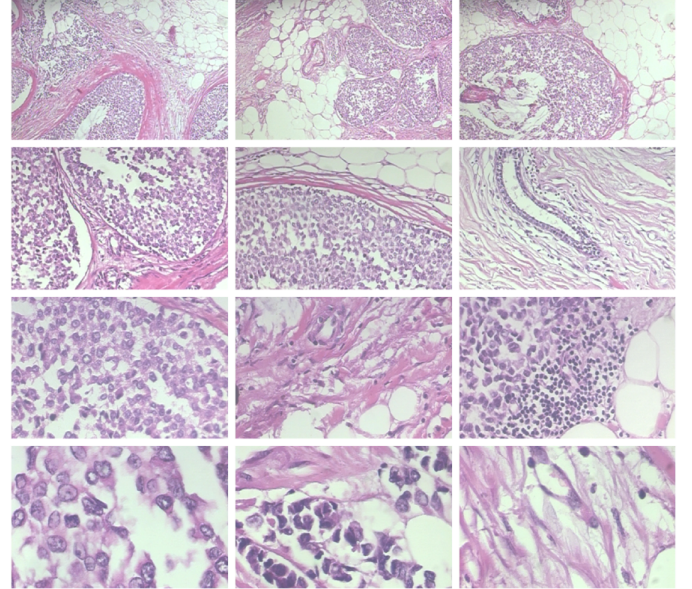


Fig. 9: Misclassified malignant samples. From top to bottom: samples seen in magnification factors of 40 \times , 100 \times , 200 \times and 400 \times respectively.

TABLE IX: Number of patches derived from the PAIP 2019 dataset.

	Normal	Tumour	Total
Training	15,000	15,000	30,000
Testing	10,000	9,375	19,375

non-overlapping cropping. We randomly select 1,000 patches per slide for training and testing purposes. The final numbers of different patches derived from the PAIP 2019 dataset are summarized in Table IX. Due to tiny viable tumour areas in some slides, the number of tumour patches for testing is 9,375 instead of 10,000.

2) *Results and discussion:* Table X lists the classification performance evaluated on the testing dataset derived from the PAIP, which compares accuracy (ACC) and $F1$ -score

of different neural networks trained in different ways. The ACC increases by a large margin from 73.6% to around 90% when the plain neural network PNN2 is trained in either the pair loss or the triplet loss. This evidences that the SMSE scheme works effectively with superior performance for tissue patch classification. Besides the ACC , same increase of $F1$ -score can be observed for network PNN2. As for more complicated neural networks like GoogleNet or ResNet with a tailor designed architecture, it can be seen that the performance from different loss functions are close since these kind of networks are powerful to extract robust features, and triplet loss introduces a small improvement in all cases.

In addition to the quantitative analysis above, t-distributed

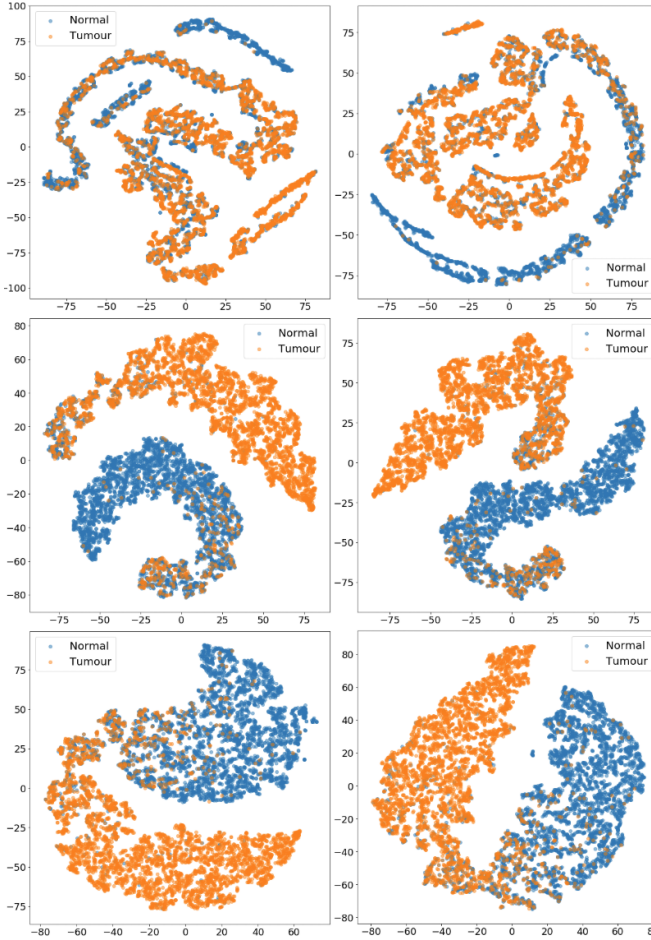


Fig. 10: A t-SNE visualization of embeddings learned from image-label data (first row), image pairs (second row) and image triplets (third row). Left: embeddings extracted from training set; right: embeddings extracted from testing set.

TABLE X: Performance comparison of liver cancer histopathological image classification.

Network	Loss function	ACC (%)	F1-score (%)	
			Normal	Tumour
PNN2	\mathcal{L}_{cls}	73.6	68.9	77.1
	$\mathcal{L}_{cls} + \mathcal{L}_p$	90.3	90.2	90.4
	$\mathcal{L}_{cls} + \mathcal{L}_t$	90.2	90.3	90.0
GoogleNet	\mathcal{L}_{cls}	93.1	93.4	92.9
	$\mathcal{L}_{cls} + \mathcal{L}_p$	92.5	92.6	92.4
	$\mathcal{L}_{cls} + \mathcal{L}_t$	93.8	94.0	93.5
ResNet	\mathcal{L}_{cls}	91.3	91.4	91.2
	$\mathcal{L}_{cls} + \mathcal{L}_p$	89.7	90.3	89.0
	$\mathcal{L}_{cls} + \mathcal{L}_t$	92.2	92.3	92.0

stochastic neighbor embedding (t-SNE) [48], an approach for dimensionality reduction, is exploited to visualize the high-dimensional features/embeddings for qualitative analysis. As illustrated in Fig. 10, the embeddings learned from image-label data look inseparable, while both embeddings learned via measuring similarity from image pairs and triplets are clustered in class and separable between classes.

V. CONCLUSION

We present a framework that leverages similarity embeddings for magnification-independent histopathological image classification. Moreover, we propose a reinforced focal loss to eliminate impact of class imbalance by including a punishing parameter λ and a suppressing parameter γ on top of the $L1$ loss function, to simultaneously increase losses of hard samples and decrease those of easy samples. Based on this framework, we train and test different network models for accurately classifying histopathological images. The challenges posed by imbalanced classes and multi-magnification variances within a histopathological image classification task is formulated as a multi-task learning process, namely, similarity-based embedding learning and classification. Comprehensive experiments have been conducted to evaluate the proposed models for breast and liver cancer histopathological image classification. Experimental results show that significant improvement is introduced by exploiting similarity-based embeddings, demonstrating the effectiveness of the similarity learning approach for cancerous diagnosis. Also, improvements made by varying combination of parameter λ and γ prove that the proposed reinforced focal loss function is effective for class imbalance. Overall, the proposed method yields outstanding performance on the BreakHis benchmark for breast cancer histopathological image classification when compared to the current state-of-the-art methods.

REFERENCES

- [1] J. Gilbertson, A. A. Patel, and Y. Yagi, “Clinical slide digitization: whole slide imaging in clinical practice experience from the university of pittsburgh,” in *Virtual Microscopy and Virtual Slides in Teaching, Diagnosis, and Research*, pp. 239–254. CRC Press, 2005.
- [2] N. Bayramoglu, J. Kannala, and J. Heikkilä, “Deep learning for magnification independent breast cancer histopathology image classification,” in *2016 23rd International conference on pattern recognition (ICPR)*. IEEE, 2016, pp. 2440–2445.
- [3] V. Gupta and A. Bhavsar, “Breast cancer histopathological image classification: is magnification important?,” in *Proceedings of the IEEE Conference on Computer Vision and Pattern Recognition Workshops*, 2017, pp. 17–24.
- [4] M. S. Reza and J. Ma, “Imbalanced histopathological breast cancer image classification with convolutional neural network,” in *2018 14th IEEE International Conference on Signal Processing (ICSP)*. IEEE, 2018, pp. 619–624.
- [5] Sudipta Acharya, Sriparna Saha, and Yamini Thadisina, “Multiobjective simulated annealing-based clustering of tissue samples for cancer diagnosis,” *IEEE journal of biomedical and health informatics*, vol. 20, no. 2, pp. 691–698, 2015.
- [6] Shancheng Jiang, Huichuan Li, and Zhi Jin, “A visually interpretable deep learning framework for histopathological image-based skin cancer diagnosis,” *IEEE Journal of Biomedical and Health Informatics*, vol. 25, no. 5, pp. 1483–1494, 2021.
- [7] S. H. Raza, R. M. Parry, R. A. Moffitt, A. N. Young, and M. D. Wang, “An analysis of scale and rotation invariance in the bag-of-features method for histopathological image classification,” in *International Conference on Medical Image Computing and Computer-Assisted Intervention*. Springer, 2011, pp. 66–74.
- [8] U. Srinivas, H. S. Mousavi, V. Monga, A. Hattel, and B. Jayarao, “Simultaneous sparsity model for histopathological image representation and classification,” *IEEE transactions on medical imaging*, vol. 33, no. 5, pp. 1163–1179, 2014.
- [9] T. Gultekin, C. F. Koyuncu, C. Sokmensuer, and C. Gunduz-Demir, “Two-tier tissue decomposition for histopathological image representation and classification,” *IEEE transactions on medical imaging*, vol. 34, no. 1, pp. 275–283, 2014.

[10] X. Zhang, H. Dou, T. Ju, J. Xu, and S. Zhang, “Fusing heterogeneous features from stacked sparse autoencoder for histopathological image analysis,” *IEEE journal of biomedical and health informatics*, vol. 20, no. 5, pp. 1377–1383, 2015.

[11] T. H. Vu, H. S. Mousavi, V. Monga, G. Rao, and U. A. Rao, “Histopathological image classification using discriminative feature-oriented dictionary learning,” *IEEE transactions on medical imaging*, vol. 35, no. 3, pp. 738–751, 2015.

[12] Jun Shi, Jinjie Wu, Yan Li, Qi Zhang, and Shihui Ying, “Histopathological image classification with color pattern random binary hashing-based pcenet and matrix-form classifier,” *IEEE journal of biomedical and health informatics*, vol. 21, no. 5, pp. 1327–1337, 2016.

[13] Q. Qi, Y. Li, J. Wang, H. Zheng, Y. Huang, X. Ding, and G. K. Rohde, “Label-efficient breast cancer histopathological image classification,” *IEEE journal of biomedical and health informatics*, vol. 23, no. 5, pp. 2108–2116, 2018.

[14] Y. Zheng, Z. Jiang, H. Zhang, F. Xie, Y. Ma, H. Shi, and Y. Zhao, “Histopathological whole slide image analysis using context-based cbir,” *IEEE transactions on medical imaging*, vol. 37, no. 7, pp. 1641–1652, 2018.

[15] Chunli Sun, Ao Xu, Dong Liu, Zhiwei Xiong, Feng Zhao, and Weiping Ding, “Deep learning-based classification of liver cancer histopathology images using only global labels,” *IEEE journal of biomedical and health informatics*, vol. 24, no. 6, pp. 1643–1651, 2019.

[16] R. Yan, F. Ren, Z. Wang, L. Wang, T. Zhang, Y. Liu, X. Rao, C. Zheng, and F. Zhang, “Breast cancer histopathological image classification using a hybrid deep neural network,” *Methods*, vol. 173, pp. 52–60, 2020.

[17] M. Gour, S. Jain, and T. S. Kumar, “Residual learning based cnn for breast cancer histopathological image classification,” *International Journal of Imaging Systems and Technology*, 2020.

[18] Raia Hadsell, Sumit Chopra, and Yann LeCun, “Dimensionality reduction by learning an invariant mapping,” in *2006 IEEE Computer Society Conference on Computer Vision and Pattern Recognition (CVPR’06)*. IEEE, 2006, vol. 2, pp. 1735–1742.

[19] Zhirong Wu, Yuanjun Xiong, Stella X Yu, and Dahua Lin, “Unsupervised feature learning via non-parametric instance discrimination,” in *Proceedings of the IEEE Conference on Computer Vision and Pattern Recognition*, 2018, pp. 3733–3742.

[20] Philip Bachman, R Devon Hjelm, and William Buchwalter, “Learning representations by maximizing mutual information across views,” *arXiv preprint arXiv:1906.00910*, 2019.

[21] Alexey Dosovitskiy, Jost Tobias Springenberg, Martin Riedmiller, and Thomas Brox, “Discriminative unsupervised feature learning with convolutional neural networks,” Citeseer, 2014.

[22] Kaiming He, Haoqi Fan, Yuxin Wu, Saining Xie, and Ross Girshick, “Momentum contrast for unsupervised visual representation learning,” in *Proceedings of the IEEE/CVF Conference on Computer Vision and Pattern Recognition*, 2020, pp. 9729–9738.

[23] Ishan Misra and Laurens van der Maaten, “Self-supervised learning of pretext-invariant representations,” in *Proceedings of the IEEE/CVF Conference on Computer Vision and Pattern Recognition*, 2020, pp. 6707–6717.

[24] Carl Doersch and Andrew Zisserman, “Multi-task self-supervised visual learning,” in *Proceedings of the IEEE International Conference on Computer Vision*, 2017, pp. 2051–2060.

[25] Mang Ye, Xu Zhang, Pong C Yuen, and Shih-Fu Chang, “Unsupervised embedding learning via invariant and spreading instance feature,” in *Proceedings of the IEEE/CVF Conference on Computer Vision and Pattern Recognition*, 2019, pp. 6210–6219.

[26] Xu Ji, João F Henriques, and Andrea Vedaldi, “Invariant information clustering for unsupervised image classification and segmentation,” in *Proceedings of the IEEE/CVF International Conference on Computer Vision*, 2019, pp. 9865–9874.

[27] E. Hoffer and N. Ailon, “Deep metric learning using triplet network,” in *International Workshop on Similarity-Based Pattern Recognition*. Springer, 2015, pp. 84–92.

[28] J. Bromley, J. W. Bentz, L. Bottou, I. Guyon, Y. LeCun, C. Moore, E. Säckinger, and R. Shah, “Signature verification using a “siamese” time delay neural network,” *International Journal of Pattern Recognition and Artificial Intelligence*, vol. 7, no. 04, pp. 669–688, 1993.

[29] G. Koch, R. Zemel, and R. Salakhutdinov, “Siamese neural networks for one-shot image recognition,” in *ICML deep learning workshop*, 2015, vol. 2.

[30] L. Bertinetto, J. Valmadre, J. F. Henriques, A. Vedaldi, and P. H. Torr, “Fully-convolutional siamese networks for object tracking,” in *European conference on computer vision*. Springer, 2016, pp. 850–865.

[31] M. Pazzani, C. Merz, P. Murphy, K. Ali, T. Hume, and C. Brunk, “Reducing misclassification costs,” in *Machine Learning Proceedings 1994*, pp. 217–225. Elsevier, 1994.

[32] N. Japkowicz, “The class imbalance problem: Significance and strategies,” in *Proc. of the Int’l Conf. on Artificial Intelligence*. Citeseer, 2000, vol. 56.

[33] S. R. Bulo, G. Neuhold, and P. Kortscheder, “Loss max-pooling for semantic image segmentation,” in *2017 IEEE Conference on Computer Vision and Pattern Recognition (CVPR)*. IEEE, 2017, pp. 7082–7091.

[34] T. Lin, P. Goyal, R. Girshick, K. He, and P. Dollár, “Focal loss for dense object detection,” in *Proceedings of the IEEE international conference on computer vision*, 2017, pp. 2980–2988.

[35] Y. Zhu, S. Zhang, W. Liu, and D. N. Metaxas, “Scalable histopathological image analysis via active learning,” in *International Conference on Medical Image Computing and Computer-Assisted Intervention*. Springer, 2014, pp. 369–376.

[36] A. Shrivastava, A. Gupta, and R. Girshick, “Training region-based object detectors with online hard example mining,” in *Proceedings of the IEEE conference on computer vision and pattern recognition*, 2016, pp. 761–769.

[37] D. P. Kingma and J. Ba, “Adam: A method for stochastic optimization,” *arXiv preprint arXiv:1412.6980*, 2014.

[38] F. A. Spanhol, L. S. Oliveira, C. Petitjean, and L. Heutte, “A dataset for breast cancer histopathological image classification,” *IEEE Transactions on Biomedical Engineering*, vol. 63, no. 7, pp. 1455–1462, 2015.

[39] T. Fawcett, “An introduction to roc analysis,” *Pattern recognition letters*, vol. 27, no. 8, pp. 861–874, 2006.

[40] E. Rublee, V. Rabaud, K. Konolige, and G. Bradski, “Orb: An efficient alternative to sift or surf,” in *2011 International conference on computer vision*. Ieee, 2011, pp. 2564–2571.

[41] V. Ojansivu and J. Heikkilä, “Blur insensitive texture classification using local phase quantization,” in *International conference on image and signal processing*. Springer, 2008, pp. 236–243.

[42] T. Ojala, M. Pietikainen, and T. Maenpää, “Multiresolution gray-scale and rotation invariant texture classification with local binary patterns,” *IEEE Transactions on pattern analysis and machine intelligence*, vol. 24, no. 7, pp. 971–987, 2002.

[43] Z. Guo, L. Zhang, and D. Zhang, “A completed modeling of local binary pattern operator for texture classification,” *IEEE transactions on image processing*, vol. 19, no. 6, pp. 1657–1663, 2010.

[44] R. M. Haralick, K. Shanmugam, and I. H. Dinstein, “Textural features for image classification,” *IEEE Transactions on systems, man, and cybernetics*, , no. 6, pp. 610–621, 1973.

[45] L. P. Coelho, A. Ahmed, A. Arnold, J. Kangas, A. Sheikh, E. P. Xing, W. W. Cohen, and R. F. Murphy, “Structured literature image finder: extracting information from text and images in biomedical literature,” in *Linking Literature, Information, and Knowledge for Biology*, pp. 23–32. Springer, 2010.

[46] C. Szegedy, W. Liu, Y. Jia, P. Sermanet, S. Reed, D. Anguelov, D. Erhan, V. Vanhoucke, and A. Rabinovich, “Going deeper with convolutions,” in *Proceedings of the IEEE conference on computer vision and pattern recognition*, 2015, pp. 1–9.

[47] K. He, X. Zhang, S. Ren, and J. Sun, “Deep residual learning for image recognition,” in *Proceedings of the IEEE conference on computer vision and pattern recognition*, 2016, pp. 770–778.

[48] L. Maaten and G. Hinton, “Visualizing data using t-sne,” *Journal of machine learning research*, vol. 9, no. Nov, pp. 2579–2605, 2008.